



# Research on quality analysis of solid-liquid two-phase abrasive flow precision machining based on different sub-grid scale models

Weihong Zhao<sup>1</sup> · Jiyong Qu<sup>1</sup> · Junye Li<sup>1,2</sup> · Ningning Su<sup>1</sup> · Guangfeng Shi<sup>1</sup> · Jianhe Liu<sup>1</sup>

Received: 21 October 2020 / Accepted: 28 June 2021 / Published online: 27 November 2021  
© The Author(s), under exclusive licence to Springer-Verlag London Ltd., part of Springer Nature 2021

## Abstract

In the traditional precision and ultra-precision machining technology field, workpieces with irregular internal curved surfaces tend to have no subsequent processing after basic machining due to the limited processing means, and the surface quality of such workpieces is often not up to standard. Precision machining of abrasive flow can effectively improve this drawback and improve the surface quality of the irregular inner curved surface. In order to propose the quality control technology of the precision machining of the irregular inner curved surface of the abrasive flow, this paper uses large eddy simulation method as research means, analyzes the precision machining mechanism of abrasive flow machining curved flow channel workpiece by four different sub-grid models, establishes a reasonable sub-grid-scale model, and analyzes the abrasive flow precision machining mechanism of spiral flow channel with this model. It is found that shear force increases with the increase of inlet pressure, the interaction effect of particles in the abrasive flow and the wall surface of the flow channel is enhanced, the turbulence and disorder effect of the fluid is improved, burrs and scratches on the surface are effectively removed, and the surface quality of the workpiece is improved. The greater the inlet pressure, the stronger the turbulence effect and the higher the processing efficiency of the abrasive flow, and the better the precision machining quality of abrasive flow. Properly increasing the inlet pressure can obtain a higher surface quality of the irregular inner curved surface workpiece.

**Keywords** Large eddy simulation · Sub-grid-scale model · Abrasive flow precision machining · Irregular inner surface · Quality control

## 1 Introduction

The finishing process of the surface of complex parts is the most time-consuming and labor-intensive [1]. With the occurrence of the industrial revolution, many automation enterprises keep improving the quality of products while bringing products closer to complexity and precision. Now the inner surfaces of molds, nozzles, impeller blades, etc. require precise dimensions and uniform surface quality. Traditional finishing processes have limited applicability and limitations, but abrasive flow machining (AFM) is a good fit for this

requirement. It forms a flow channel by the workpiece itself or the fixture and flows the abrasive through the surface of the workpiece at a certain pressure to complete the finishing. The schematic diagram of abrasive flow machining is shown in Figure 1.

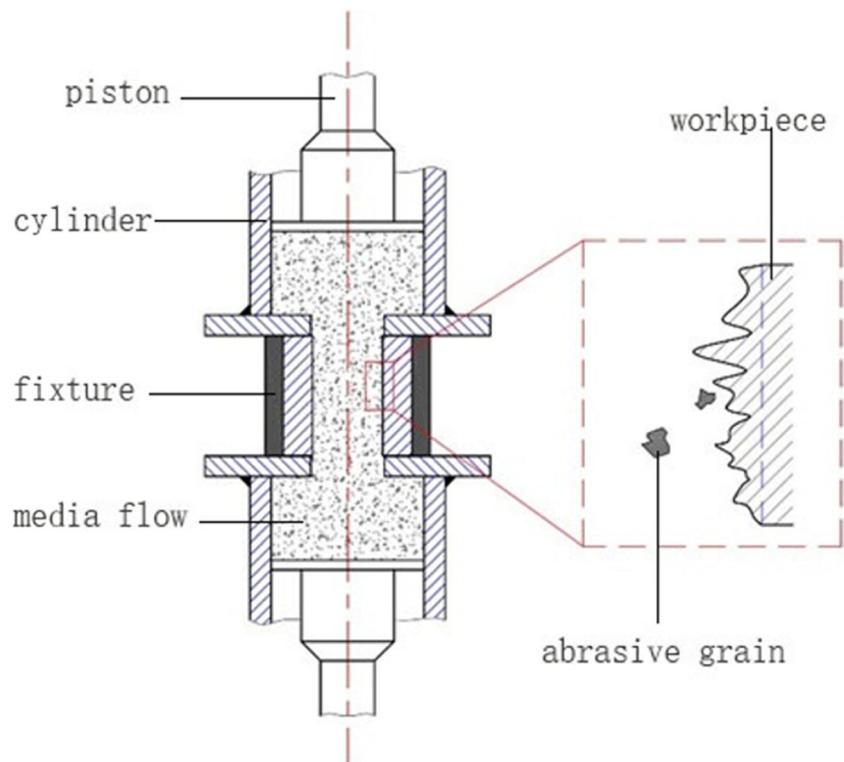
Abrasive flow machining technology has been applied in many fields, and many researchers at home and abroad have done a lot of research on it. Sato et al. [2] have studied the effect of medium degradation on the characteristics of abrasive flow machining. The results show that medium degradation does not have much influence on surface roughness. Sankar et al. [3] proposed a rotatable abrasive flow machining technology for the problem of low efficiency of abrasive flow machining. Experiments on AISI 4340 tubes were carried out. The results show that the surface quality is significantly improved. Fu et al. [4] studied the blade through experiments and numerical simulations and analyzed the case of the abrasive flow machining with and without guide blocks, and the uniformity of abrasive flow machining increased by 26.9%. Duval-Chaneac et al. [5] studied the polishing of parts processed by selective laser melting of maraging steel 300 without heat treatment and heat

✉ Junye Li  
ljy@cust.edu.cn

<sup>1</sup> Ministry of Education Key Laboratory for Cross-Scale Micro and Nano Manufacturing, Changchun University of Science and Technology, Changchun 130022, China

<sup>2</sup> Changchun University of Science and Technology Chongqing Research Institute, Chongqing 401135, China

**Fig. 1** Schematic diagram of the precision machining of abrasive flow



treatment using four different abrasive flow media. The results show that the surface roughness depends on the viscosity and concentration of the medium, and can be reduced to  $2\ \mu\text{m}$ . Singh et al. [6] proposed a new simulation model for different AFF processing parameters to predict the roughness on the surface of microporous walls. Li et al. [7] used the large eddy simulation method to study the surface formation mechanism of the solid-liquid two-phase abrasive flow process.

Silvis et al. [8] have studied the construction of sub-grid-scale models for large eddy simulation of incompressible turbulent flows. Zhang et al. [9] have performed large eddy simulation (LES) in a channel with a rough wall on one side and a free surface on the other by adopting an anisotropy-resolving sub-grid-scale (SGS) model. Linkmann et al. [10] provided analytical and numerical results concerning multi-scale correlations between the resolved velocity field and the sub-grid-scale (SGS) stress tensor in large eddy simulations (LES). Mao et al. [11] used a large eddy simulation (LES) method with different sub-grid-scale models to numerically study the magnetohydrodynamics (MHD) turbulent duct flow.

Abrasive flow machining technology, as a soft machining method, uses micro-cutting and micro-collision of particles to effectively remove surface impurities and improve the surface quality and surface smoothness and do not generate stress concentration [12]. The machining state of the abrasive flow is characterized by turbulence, which helps to achieve micro-cutting of complex surfaces with a small force [13]. In the existing research, the sub-grid model is rarely analyzed and

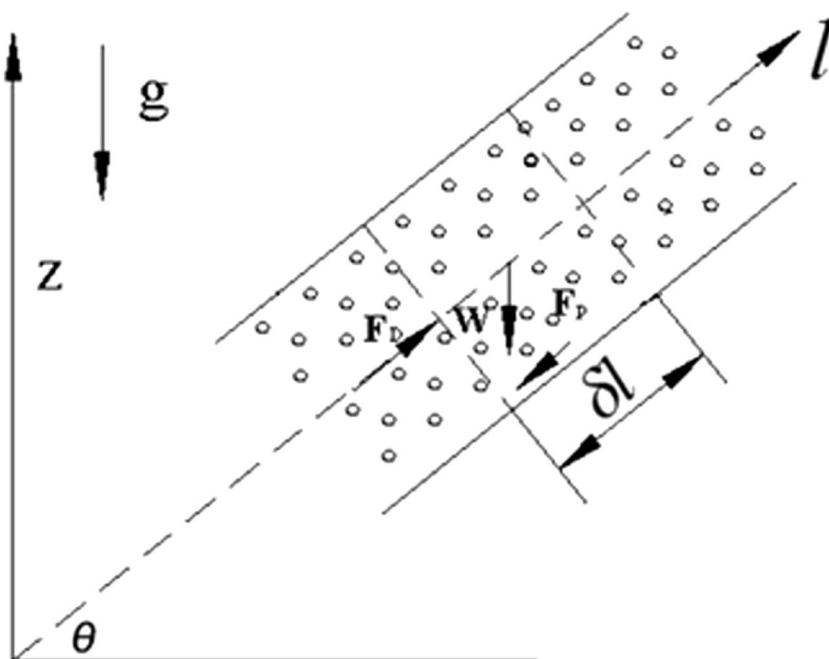
discussed. In this paper, the irregular inner curved surface is taken as the structural object, and the large eddy simulation method is used to analyze the numerical results of different sub-grid-scale models for abrasive flow machining, and the appropriate sub-grid-scale model is determined. Then the model is used to numerically analyze the machining parameters of the abrasive flow, revealing the precise machining mechanism of the abrasive flow, and finally the experimental analysis of the irregular inner curved surface parts.

## 2 Particle motion analysis of solid-liquid two-phase abrasive flow precision machining

### 2.1 Differential equations of motion for particle groups

Because the flow of the particle group in the elbow and spiral tube with complex cross-sections is more complicated, in order to better understand the movement of the particle group, the circular section pipe is taken as an example for analysis. The inner diameter of the pipe is  $d$ , the inclination angle is  $\theta$ , and the abrasive flow flows in the  $l$  direction inside. The schematic diagram of the movement of the solid-liquid two-phase abrasive flow in the inclined pipe is shown in Figure 2. The solid-liquid two-phase abrasive flow is uniform flow during the movement, and the two phases are uniformly mixed. The following assumptions are made: it is assumed that during the

**Fig. 2** Movement of solid-liquid two-phase abrasive particle flow in the inclined pipe



flow process, the advancement velocity  $v_p$  of the particle group remains the same, and the average velocity of the cross-section of the liquid phase is  $v_l$ ; the forces acting on the particles have primary force and secondary force, and only the three main forces acting on the particles are considered, namely the resistance exerted by the liquid on the particles, the gravity of the particles themselves, and the friction force between the particles and between the particles and the wall surface. Let the two sections of the distance  $\delta l$  (shown by the dashed line in Figure 2) and the wall between the sections be the control surface, and  $F_D$ ,  $W$ , and  $F_p$  are respectively represented as the resistance of the liquid acting on the particle group, the gravity of the particle group, and the friction force between the wall surface and the particle group in the control body; then the motion differential equation of the particle group in the control body is:

$$F_D - W \sin \theta - F_p = q_{mp} \frac{\delta l}{v_p} \frac{dv_p}{dt} \tag{1}$$

where  $q_{mp}$  is the mass flow rate of the solid phase.

If the diameter of the particles in the control body is  $d_p$ , the total number is  $N$ , the particle concentration is  $\rho_p'$ , and the resistance is  $f_D$  of the liquid acting on each particle, the hydrodynamic resistance of the liquid acting on the particle group is:

$$F_D = N f_D = \frac{6}{\pi d_p^3} \frac{\rho_p' A \delta l}{\rho_p} \times C_D \frac{\rho_l (v_l - v_p)^2}{2} \frac{\pi d_p^2}{4} \tag{2}$$

$$= C_D \frac{3 \rho_l v_p q_{mp}}{4 \rho_p d_p} \left( \frac{v_l}{v_p} - 1 \right)^2 \delta l$$

where  $A$  flows through the area,  $\rho_l$  is the liquid phase density,  $v_l$  is the liquid phase velocity,  $\rho_p$  is the solid phase density, and  $C_D$  is the drag coefficient.

Assuming that buoyancy can be ignored, the gravity of the visible particle group is equal to the hydrodynamic resistance when they freely settle, namely:

$$W = q_{mp} \frac{\delta l}{v_p} g = N f_{Df} = \frac{6}{\pi d_p^3} \frac{\rho_p' A \delta l}{\rho_p} \times C_{Df} \frac{\rho_l v_f^2}{2} \frac{\pi d_p^2}{4} \tag{3}$$

$$= C_{Df} \frac{3 \rho_l v_f^2 q_{mp}}{4 \rho_p d_p v_p} \delta l$$

where  $C_{Df}$  is the hydrodynamic drag coefficient when the particles fall at a free settling velocity  $v_f$  and  $f_{Df}$  is the resistance of liquid acting on each particle when the particle is free to settle.

In the precision machining process, since the particle diameter in the abrasive flow is minimal, generally several tens of micrometers, it is almost impossible to accurately describe the friction between the wall surface and the particle group. Since the particles are uniformly dispersed in the liquid medium, they are considered pseudo-fluid, so the friction force between the wall surface and the particle group can be expressed as the friction between the wall surface and the fluid:

$$F_p = \lambda_p \frac{\delta l}{d} \frac{\rho_p' v_p^2}{2} \frac{\pi d^2}{4} \tag{4}$$

where  $\lambda_p$  is the energy loss coefficient along the path of the particle pseudo-fluid.

The drag coefficients in Equations (2) and (3) can be written in the Blasius formula:

$$C_D = \frac{c}{\text{Re}^n} = c \left[ \frac{\rho_l (v_l - v_p) d_p}{\mu_l} \right]^{-n} \quad (5)$$

$$C_{Df} = \frac{c}{\text{Re}_f^n} = c \left( \frac{\rho_l v_f d_p}{\mu_l} \right)^{-n} \quad (6)$$

$$\frac{C_{Df}}{C_D} = \left( \frac{\text{Re}}{\text{Re}_f} \right)^n = \left( \frac{v_l - v_p}{v_f} \right)^n \quad (7)$$

where  $\text{Re}$ ,  $\text{Re}_f$  is the Reynolds number of the particles and  $\mu_l$  is the liquid phase viscosity.

Substituting Equation (7) into Equation (3) yields:

$$W = q_{mp} \frac{\delta l}{v_p} g = C_D \frac{3\rho_l v_f^2 q_{mp}}{4\rho_p d_p v_p} \left( \frac{v_l - v_p}{v_f} \right)^n \delta l \quad (8)$$

Then there are:

$$C_D = \frac{4\rho_p d_p g}{3\rho_l} \frac{v_f^{n-2}}{(v_l - v_p)^n} \quad (9)$$

Substituting Equations (2), (4), (8), and (9) into Equation (1), taking the limit of  $\delta l \rightarrow 0$ , the differential equation of motion of the particle group is obtained:

$$\left( \frac{v_l - v_p}{v_f} \right)^{2-n} - \sin\theta \frac{\lambda_p v_p^2}{d} \frac{1}{2g} = \frac{1}{g} \frac{dv_p}{dt} \quad (10)$$

Since the particle velocity is  $v_p = dl/dt$ , there is  $dt = dl/v_p$ , and substituting into Equation (10) yields:

$$\left( \frac{v_l - v_p}{v_f} \right)^{2-n} - \sin\theta \frac{\lambda_p v_p^2}{d} \frac{1}{2g} = \frac{v_p dv_p}{g dl} \quad (11)$$

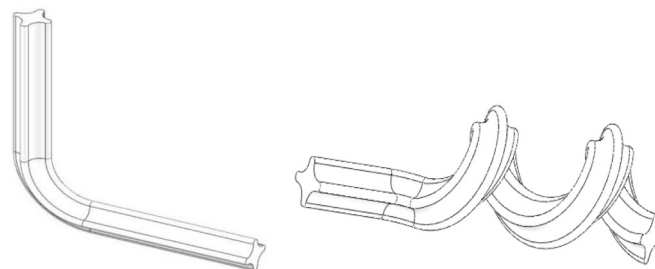
Let  $\dot{v}_p = v_p/v_l$ ,  $Fr = \frac{v_l}{(gd)^{1/2}}$ , and  $Fr_f = \frac{v_f}{(gd)^{1/2}}$ , then (11) can be written as:

$$\begin{aligned} & \left( 1 - \dot{v}_p \right)^{2-n} - \left( \frac{Fr_f}{Fr} \right)^{2-n} \sin\theta \frac{\lambda_p Fr_f^{2-n} Fr^n v_p^2}{2} \\ & = Fr_f^{2-n} Fr^n v_p \frac{dv_p}{d(l/d)} \end{aligned} \quad (12)$$

where  $Fr$ ,  $Fr_f$  is the Froude number.

The above equation is a zero-dimensional particle group motion differential equation, namely the criterion equation.

**Fig. 3** The internal structure of the flow channel. **a** Internal structure of curved channel. **b** Internal structure of spiral flow channel



(a) Internal structure of curved channel

(b) Internal structure of spiral flow channel

By analyzing the equation of motion of the solid-liquid two-phase abrasive flow particle group in the inclined pipe, the influencing factors of the force between particles and wall surface in abrasive particle flow are understood, which provides the basis for results analysis of large eddy simulation of abrasive flow precision machining of the irregular curved tube.

### 3 Analysis and discussion

#### 3.1 Numerical analysis of precision machining of solid-liquid two-phase abrasive flow

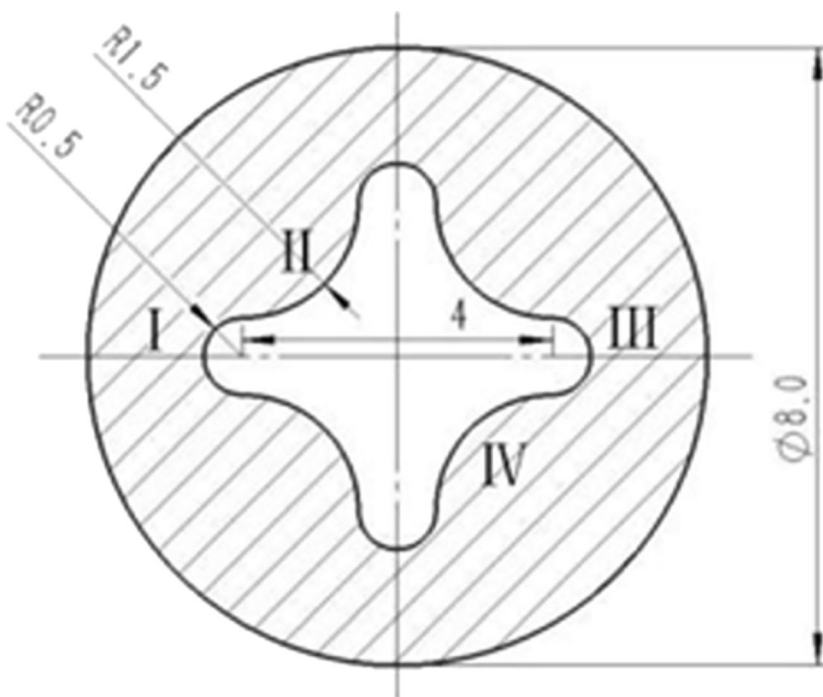
##### 3.1.1 Establishment of a numerical analysis model for abrasive flow machining

The elbow pipe structure with an irregular inner surface is selected as the research object. The elbow pipe is made of 304 stainless steel, which is universal stainless steel with a tensile strength of 515~1035MPa and has the characteristics of excellent processability and high toughness. The diameter of the semicircle at the channel groove is 1mm, the distance between the two centers of the opposite semicircles is 4mm, the radius of the transition arc between the adjacent two semicircles is 1.5mm, the diameter of the outer circle of the elbow pipe is 8mm, and the four positions of the cross-section are labeled as I, II, III, and IV, respectively. To facilitate the observation of the internal structure of the flow channel, the internal structure is extracted. The internal structure of the flow channel, cross-sectional size, and position division are shown in Figure 3 and Figure 4.

The grid has a significant influence on the calculation results. If the grid is too dense, the calculation cost will increase. If the grid is too sparse, the calculation result will be inaccurate. Therefore, the grid independence test is required before the numerical calculation [14–16].

Table 1 shows that the change of the numerical calculation results is minimal, and the rate of change is within 5%, indicating that the number of units of the minimum grid of the flow channel has satisfied the calculation requirement. Therefore, the mesh division of the flow channel adopts the

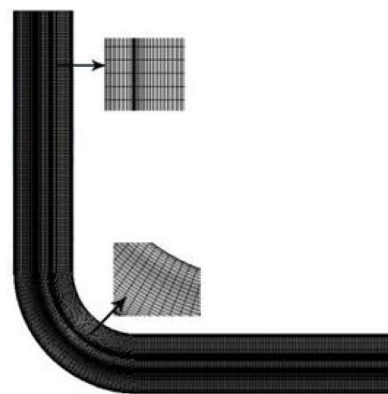
**Fig. 4** Schematic diagram of cross-sectional size and position division



minimum number of mesh units, which are 277,000 and 244,000, respectively, and the divided curved flow channel grid and spiral flow channel grid are shown in Figure 5.

According to the working principle of precision machining of abrasive flow and the proportion of actual abrasive, the solver is selected as 3D double-precision unsteady pressure solver, the multiphase flow model is a mixture model, the solid phase of the abrasive flow is silicon carbide particles, the density is 3170kg/m<sup>3</sup>, the liquid phase is oil, the density is 1260kg/m<sup>3</sup>, and the flow field is solved by combining the pressure-velocity coupling SIMPEC algorithm. In the precision machining process of the abrasive flow, the workpiece is processed by the extrusion of the piston rod, so the boundary conditions are the pressure inlet and the pressure outlet, and the pressure outlet is the standard atmospheric pressure. The discrete method uses the finite volume method for discrete, the momentum equation uses the boundary center difference format, the volume fraction

adopts the first-order upwind style, and the transient equation uses the second-order implicit format.



(a) Curved flow channel grid diagram



(b) Spiral flow channel grid diagram

**Table 1** Grid independence test results

Maximum	Number of grid units (10 <sup>5</sup> )					
	Curved channel			Spiral channel		
	27.7	34.6	61.4	24.4	40.1	61
Static pressure (10 <sup>5</sup> Pa)	1.10	1.14	1.12	5.12	5.34	5.31
Dynamic pressure (10 <sup>5</sup> Pa)	1.62	1.59	1.60	2.39	2.42	2.45
Velocity (m/s)	14.9	14.8	14.9	18.2	18.3	18.4

**Fig. 5** Schematic diagram of meshing. **a** Curved flow channel grid diagram. **b** Spiral flow channel grid diagram

### 3.1.2 Abrasive flow precision machining quality control analysis based on a sub-grid-scale model

The four commonly used sub-grid-scale models are Smagorinsky model [17], wall-adapting local eddy-viscosity (WALE) model [18], algebraic wall-modeled LES (WMLES) model [19], and dynamic kinetic energy sub-grid-scale (KET) model [20]. The sub-grid-scale model is used to analyze the precision machining characteristics of the abrasive flow, and the optimal sub-grid-scale model of abrasive flow machining is obtained.

#### (1) Analysis and selection of sub-grid-scale model

Due to the complicated flow field changes in the flow channel, it is difficult to describe the flow distribution and flow state of the abrasive flow, and the changing trend of the internal flow field cannot be observed by a single section. Therefore, multiple sections are needed for auxiliary observation to analyze the flow field in detail. According to the literature review, the surface quality of the workpiece is mainly affected by the pressure difference, and the precision machining effect of the abrasive flow is better at 2 MPa, so the

pressure inlet is set to 2 Mpa, and the outlet is atmospheric pressure. The streamlined distribution of different sub-grid-scale models is shown in Figure 6.

It can be seen from the streamline distribution of different sub-grid-scale models that only the WALE and KET sub-grid-scale models appear vortex on the inner side of the right angle of the workpiece, and the other two sub-grid-scale models do not appear. It can be seen from Figure 6b that the streamlines do not change at the behind of the vortex and flow out directly along the flow channel, and the vortex is generated near the wall surface without turbulent boundary layer, the turbulent near-wall characteristics are not obvious, there is no fluid supplement in the vortex motion, and the vortex generation is unclear. In contrast, Figure 6d shows different behavior. There is a change of direction behind the vortex. This is because the fluid will disintegrate to the inner side after colliding with the outside of the right angle, and the fluid colliding with the inner side is divided into two streams, one stream is the vortex, and there is a turbulent boundary layer between the vortex and the wall surface, the turbulent boundary layer fluid flows in the reverse direction, and the boundary layer fluid interacts with the mainstream to form vortex. The other will change its

**Fig. 6** Streamline diagram of four sub-grid-scale models. **a** Smagorinsky model. **b** WALE model. **c** WMLES model. **d** KET model

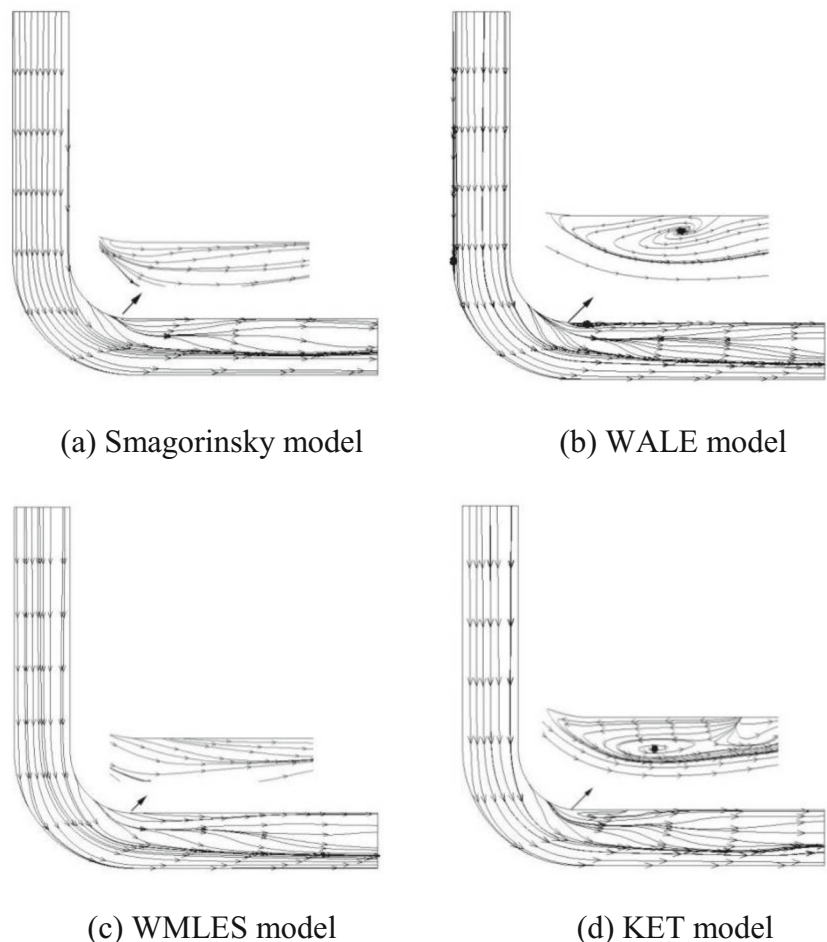
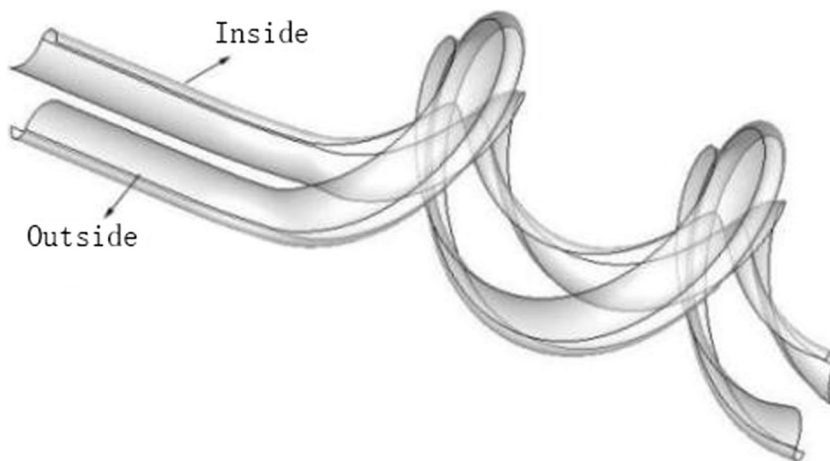


**Fig. 7** Schematic diagram of the positional division of the inner wall surface of the spiral flow channel



route due to impact and then move on. KET model has better simulation results than the WALE model.

According to the numerical analysis of different sub-grid-scale models, the KET model has higher simulation precision and has a higher capturing ability for flow field details and weak pulsation scales, indicating that the KET model has better simulation results for the fluid.

(2) Quality control analysis of sub-grid-scale model for precision machining of the spiral channel by abrasive flow

According to the analysis of the precision machining mechanism of the abrasive flow in the curved flow channel by using four different sub-grid-scale models, the KET sub-grid-scale model is selected to calculate the spiral flow channel. Since the pressure plays a large role in the machining effect of the abrasive flow, the pressure parameter is selected to numerically simulate it. According to the relevant literature, the theoretical analysis of the pressure required for surface burr removal shows that the surface quality changes obviously between 1 and 4 MPa, and then the pressure parameters of 2Mpa, 3Mpa, and 4Mpa are selected according to the pressure of the processing system. The structure of the spiral flow channel is complicated, and the wall surface machining effect at the near center and the

telecentric point is inconsistent. Therefore, to facilitate the numerical comparison, the wall surfaces of the near center (inside) and far away from the center (outside) are selected for comparative analysis. The schematic diagram of the positional division of the inner wall surface of the spiral flow channel and the nephogram of wall shear force changes under different inlet pressures are shown in Figure 7 and Figure 8.

It can be seen from Figure 8 that the changing trend of the wall shear force under three different inlet pressures is the same. When the fluid just enters the flow channel, friction occurs with the wall surface, and the kinetic energy is gradually reduced, so the wall shear force is also reduced in the flow channel; when the flow channel structure changes from a straight channel to a spiral channel, the fluid motion state changes, the abrasive flow collides with the wall strongly, and the wall shear force increases; when the fluid moves in the spiral flow channel, the motion state is gradually stable, the fluid energy is gradually reduced, and the shear force on the wall is also gradually reduced. However, it can be found that when the inlet pressure is 2MPa, the blue part of the wall shear force in the direct flow channel area is larger, indicating that most of the wall stress is smaller. When the inlet pressure is 4MPa, the blue part decreases, and the overall wall shear force value increases, indicating that the increase of pressure

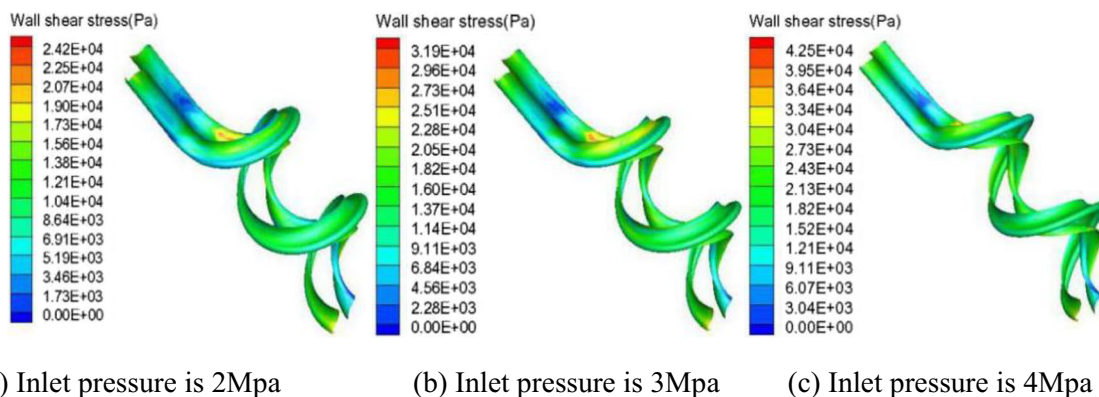


**Fig. 8** Nephogram of wall shear force changes under different inlet pressures. **a** Inlet pressure is 2Mpa. **b** Inlet pressure is 3Mpa. **c** Inlet pressure is 4Mpa

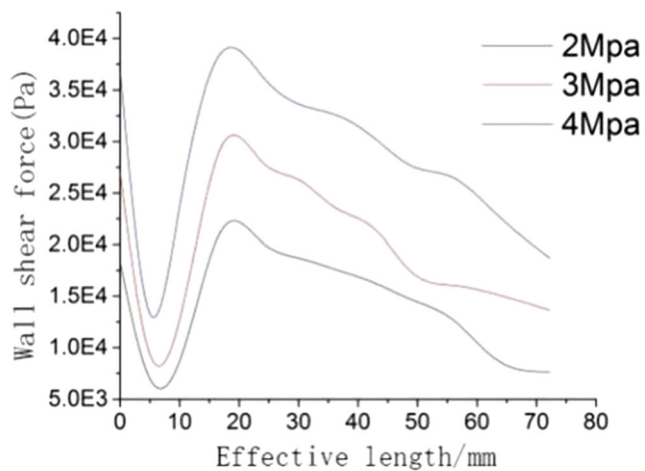


**Fig. 9** Graph of wall shear force under different inlet pressures

reduces the uneven stress phenomenon and improves the effect of abrasive flow on the wall. According to the relevant literature [21–24], the increase of the wall shear force is helpful to improve precision machining efficiency, remove hard burrs, achieve better precision machining effect of abrasive flow, and obtain better surface quality.

Figure 9 shows the wall shear force distribution curve at different inlet pressures, and the variation law of the curve also confirms the analysis of the fluid motion process in the shear force nephogram, so it is not repeated. It can also be found that in the low valley of the wall shear force curve, the curve with the pressure of 4MPa is steeper than that with the pressure of 2MPa, and the range of the smaller value of the wall shear force is small, which indicates that the greater the pressure is, the greater the force of abrasive flow on the wall is; at the position of the spiral surface, due to the continuous friction between the abrasive flow and the wall surface, as the flow path is lengthened, the pressure and kinetic energy are also gradually reduced, resulting in a decrease in the wall shear force and the reduction of the precision machining quality of the abrasive flow. The increase of inlet pressure will cause the increase of wall shear force and the increase of collision and friction between abrasive flow and wall surface, which is helpful to improve precision machining efficiency, remove hard

burrs, achieve better precision machining effect of abrasive flow, and obtain better surface quality.

In order to analyze the particle trace movement law of the abrasive flow in the precision machining process, the cross-section analysis of the spiral flow channel is carried out with the calculation result of the inlet pressure of 3Mpa. The cross-sectional division diagram and the flow trace distribution diagram are shown in Figure 10 and Figure 11.

From Figure 11, it can be seen that as the structure of the flow channel changes, the distribution position of the vortex and the size of the vortex change. Vortex is randomly distributed in the straight section where section 1-1 is located, and large vortex and small vortex coexist. This is because the abrasive flow in this section of the flow channel has less collision with the wall surface, and the small vortex energy is hardly dissipated. From sections 1-1 to 2-2, the straight flow channel is changed into a spiral flow channel, and the motion track of the abrasive flow is changed from random vortex flow to co-directional flow, because the linear structure suddenly changes into a spiral structure, and the abrasive grain flow follows the direction of the flow channel, so the same direction flow of the abrasive grain flow from the outside to the inside occurs. As the structure of the flow channel changes, the abrasive flow collides with the wall surface, and the small vortex energy depletes and the large vortex plays a leading role. From section 2-2 to section 8-8, the vortex distribution exhibits an upper-left-middle-right-upward distribution with a direction of motion counterclockwise, and the flow direction of the abrasive flow itself is also counterclockwise, which is related to the spiral structure of the flow channel. The abrasive flow enters the spiral flow channel and collides with the wall surface to generate a vortex. Since the direction of the flow channel is counterclockwise, the abrasive flow follows counterclockwise. Under the guidance of the spiral direction, the abrasive flow itself also flows counterclockwise, and the spiral direction of the flow channel and the spiral flow of the abrasive particle flow itself drive the vortex to make the spiral motion, so the motion direction of the vortex is also counterclockwise. The vortex is mainly

**Fig. 10** Schematic diagram of sectional division

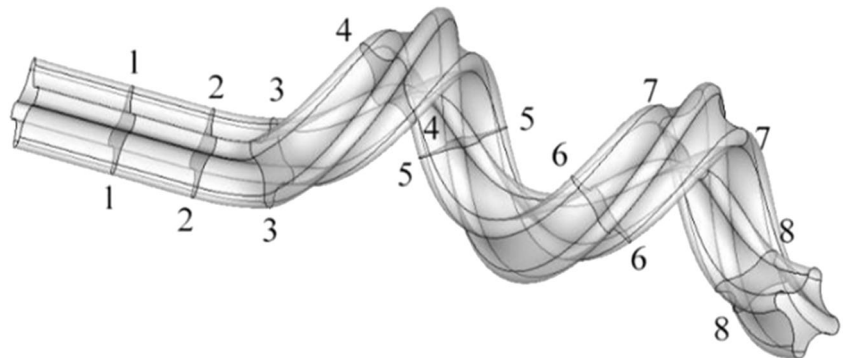
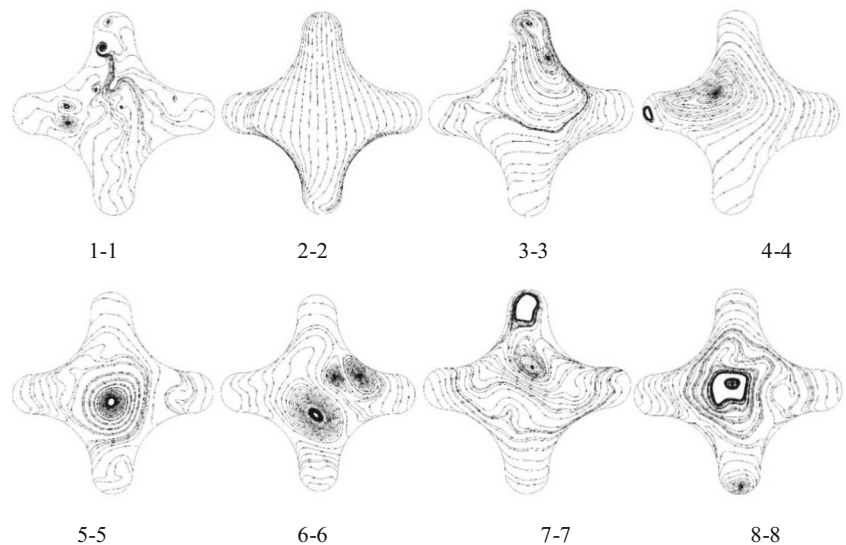




Fig. 11 Fluid trace diagram



distributed on the upper right side of the cross-section because of the centrifugal force. Because centrifugal force exerts an outward stretching force on the vortices in the process of vortices motion, the motion trajectories of the vortices are inclined to the upper right side, and small vortices hardly exist in the process of motion, which is the result of constant interaction between the abrasive flow and the wall surface, so the effect of the abrasive flow on the outer side is better than that on the inner side.

### 3.2 Test analysis

#### 3.2.1 Establishment of the test plan

The spiral channel workpiece is selected as the test workpiece, and the material of the workpiece is 304 steel. The experiment uses three factors and three levels of orthogonal test. The polishing times of abrasive flow are selected as the third factor, and the respective levels of the three parameters are as follows: inlet pressure, 2Mpa, 3Mpa, and 4 MPa; abrasive concentration, 10%, 15%, and 20%; and polishing times, 150 times, 200 times, and 250 times. The specific parameters of the orthogonal test are shown in Table 2.

The orthogonal test table designed according to the orthogonal experimental design principle is shown in Table 3.

#### 3.2.2 Analysis and discussion of orthogonal test results

The test workpieces are numbered as 01#, 02#, 03#, 04#, 05#, 07#, 08#, and 09#, and the unprocessed workpiece is marked as the original part. The wire cutting machine is applied to cut the workpieces along the axial direction and then clean them and select relevant instruments to complete the detection work.

##### (1) Detection and analysis of surface roughness

Combined with the numerical analysis results of the wall shear force of the spiral flow channel, the German Mahr LD 120 stylus measuring instrument is used to detect the surface roughness of the minimum and maximum wall shear force values at the position I of the cut part. The position of the minimum shear force on the wall is represented by A, and the position at the maximum shear force on the wall is represented by B.

Through Figure 12, it is found that the roughness values of the original workpiece at the minimum wall shear force A and the maximum wall shear force B are 3.820 and 3.763, respectively, and the surface quality of the workpiece is poor. With the gradual increase of inlet pressure and polishing times, the remaining protrusions, dents, and burrs on the surface of the

Table 2 Test parameter distribution table

Level	Factor		
	Inlet pressure (Mpa)	Polishing times (time)	Abrasive concentration (%)
1	2	150	10
2	3	200	15
3	4	250	20

**Table 3** Orthogonal test distribution table

factor Numbering	level	Polishing times		
		Inlet pressure (Mpa)	(time)	Abrasive concentration (%)
01#		2	150	10
02#		2	200	15
03#		2	250	20
04#		3	150	15
05#		3	200	20
06#		3	250	10
07#		4	150	20
08#		4	200	10
09#		4	250	15

workpiece are effectively removed, and the surface becomes more smoother. The roughness values of the workpiece 08# at A and B have been reduced to 0.631 and 0.460, respectively, and there is still a certain difference between the two positions. This phenomenon is consistent with the above wall shear force curve. However, as the inlet pressure increases, the difference between the two positions gradually decreases, and the overall polishing effect of the workpiece surface is getting better and better.

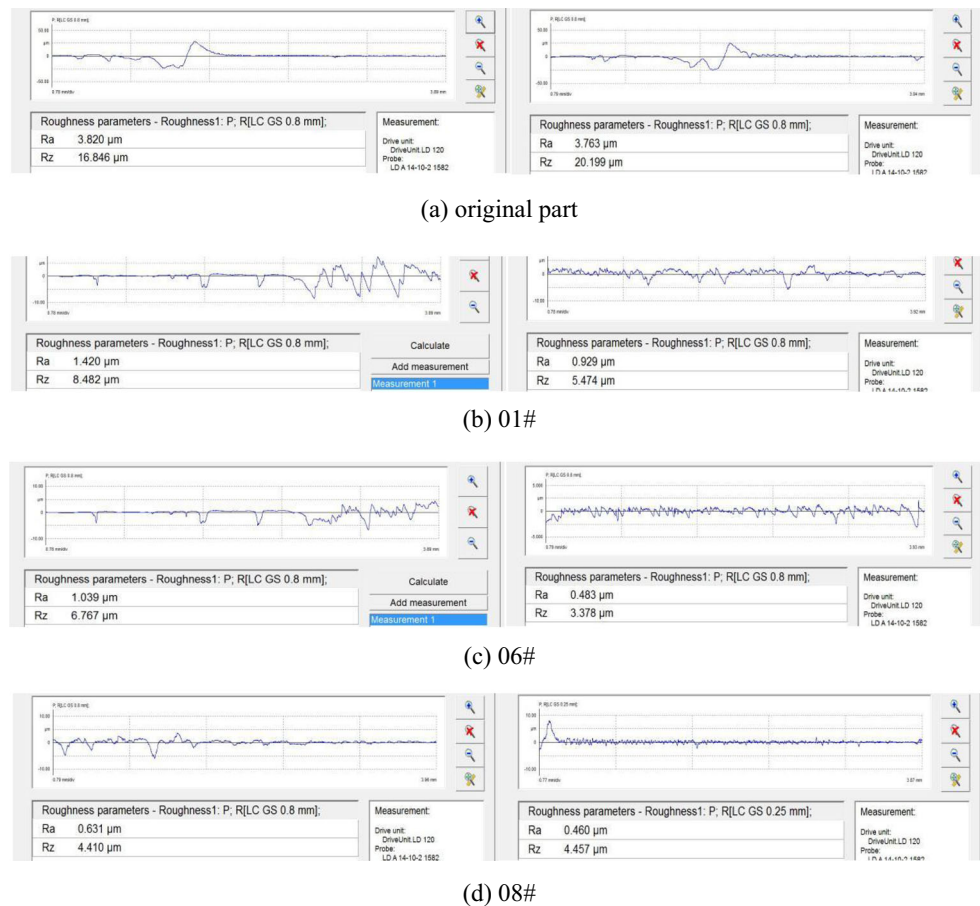
## (2) Analysis of scanning electron microscope

Taking into account the influence of eddy current in the flow path trace diagram on the machining effect and the convenience and accuracy of the workpieces detection results, the wall near the center (inside) and far away from the center (outside) of the workpiece section 5-5 is selected as the test target, and the German ZEISS EVO MA25 scanning electron microscope is used to detect the surface morphology at the same position before and after machining. The 500 times enlarged surface topography is shown in Figure 13.

It can be seen from Figure 13 that there are many protrusions, pits, and burrs on the surface of the original workpiece,

and some of the surfaces are accompanied by burns. After machining, the burning phenomenon on the surface of the workpiece has disappeared, and the surface quality of the workpieces 01#, 02#, 03#, and 06# has been greatly improved, but the surface scratch remains obvious; the number and depth of scratches on the surface of the workpiece 04# are significantly reduced; the workpiece 05# basically achieves a smooth surface, but small pits remain on the surface; the workpieces 07#, 08#, and 09# have reached the ideal surface machining effect. By analyzing the inside and outside surface topography, it can be found that the machining effect of abrasive flow on the outside is better than that on the inside, which is consistent with the analysis results of the above wall shear force nephogram and eddy current trace graph. By observing the workpieces 03#, 05#, and 07#, it can be found that the difference of machining effect on both sides gradually decreases with the increase of the inlet pressure. It can also be found that the polishing times decrease while the inlet pressure increases, and the surface obtained is still getting more and more, indicating that the influence of the inlet pressure on the quality of the machined surface is greater than the polishing times. By observing the workpieces 02#, 05#, and 08#, it can be found that with the increase of inlet pressure, better surface quality can be obtained under the condition of constant

**Fig. 12** Workpiece surface roughness inspection chart. **a** Original part, **b** 01#, **c** 06#, and **d** 08#



polishing times. Among them, the protrusions on the workpiece 08# surface are smoothed and the burrs also disappeared, becoming more smoother. Combined with Table 3, it is found that the abrasive concentration decreases as the pressure increases, but the surface quality obtained is still improving, indicating that the influence of the inlet pressure on the surface quality is greater than the abrasive concentration. Therefore, increasing the machining pressure is an efficient method to improve the abrasive flow machining effect. Comparing the 04#, 05#, and 06# group and 07#, 08#, and 09# group workpieces under the same processing pressure, it can be found that the abrasive concentration has a greater influence on the machining effect than the number of polishing times. It can be obtained that the influence of the above three factors on the processing effect is inlet pressure > abrasive concentration > polishing times.

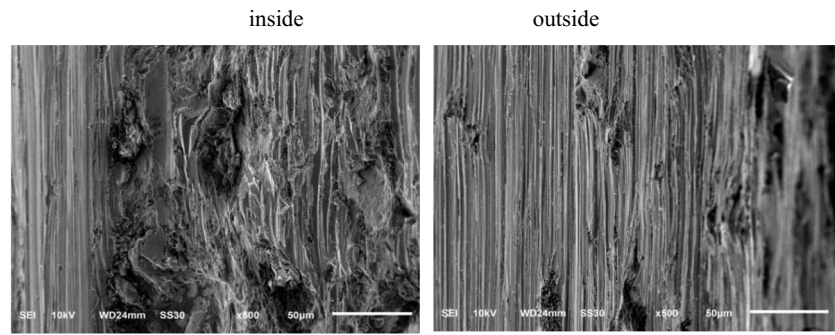
## 4 Conclusion

This paper takes the spiral flow channel workpiece as the research goal, combined with large eddy numerical simulation and experimental processing methods, explores the precision machining effect of abrasive flow machining technology on

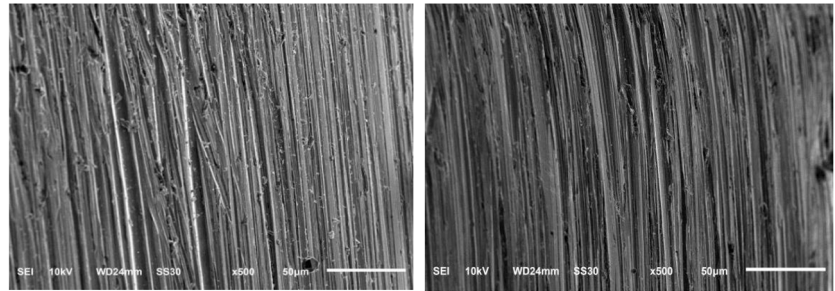
complex inner curved workpieces, and draws the following conclusions:

- (1) The numerical analysis results of KET, Smagorinsky, WALE, and WMLES models on abrasive flow machining curved runners show that the KET model has a stronger ability to capture flow field details and weak dynamic changes.
- (2) The numerical analysis results of abrasive flow machining spiral flow channel show that with the increase of inlet pressure, the polishing quality of workpiece wall surface also increases; the change of the workpiece structure has a greater impact on the position and size of the eddy current in the flow channel; the large vortex in the spiral channel plays a leading role, and its direction of rotation is affected by the spiral direction of the flow channel, which is also counterclockwise. The machining effect on the outside is better than that on the inside, which reveals the abrasive flow trajectory in the spiral channel.
- (3) Orthogonal experiment found that the influence of processing factors on the polishing effect of abrasive flow is that the inlet pressure > abrasive concentration > polishing times. And the reasonable design of processing factors is an efficient method to improve the polishing effect.

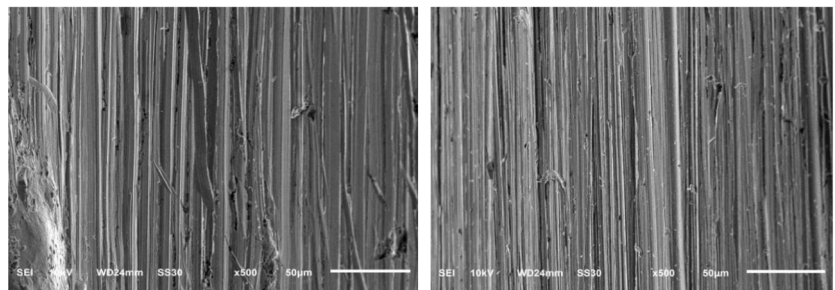
**Fig. 13** Workpiece surface topography inspection chart. **a** Original part, **b** 01#, **c** 02#, **d** 03#, **e** 04#, **f** 05#, **g** 06#, **h** 07#, **i** 08#, and **j** 09#



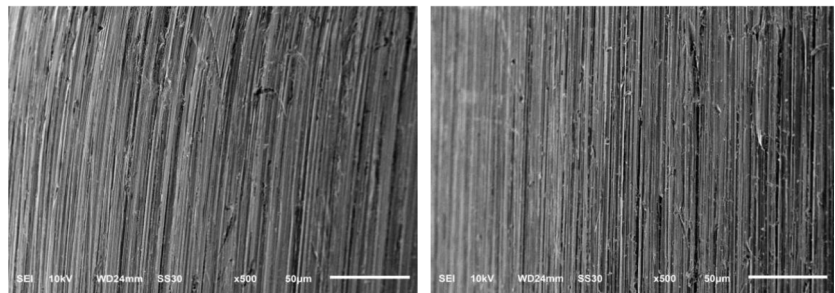
(a) original part



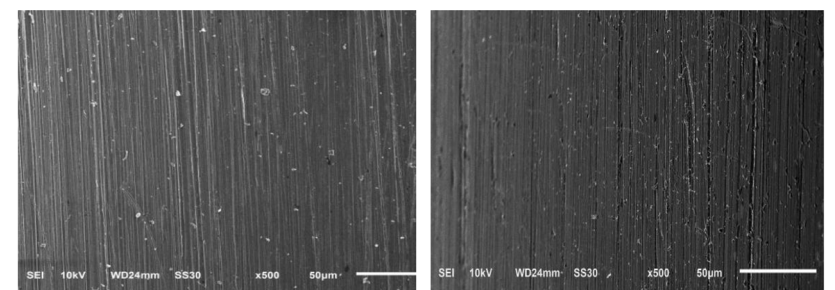
(b) 01#



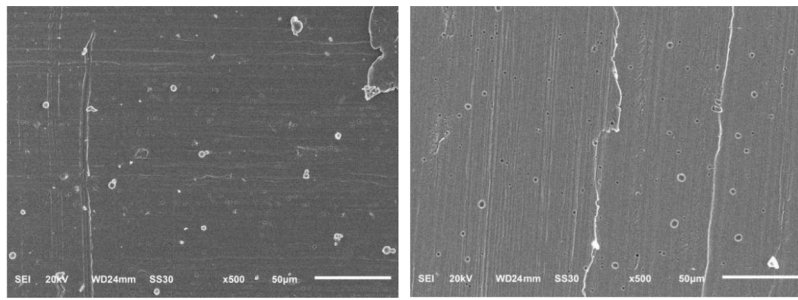
(c) 02#



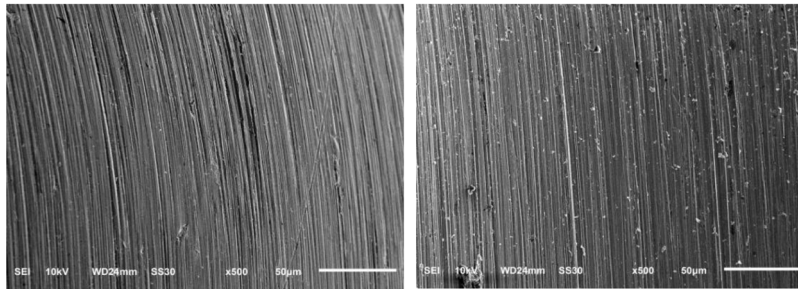
(d) 03#



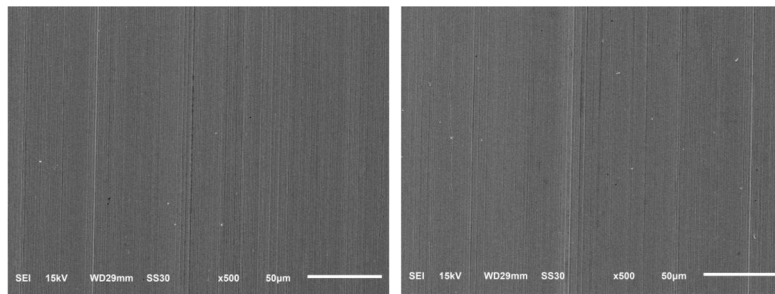
(e) 04#



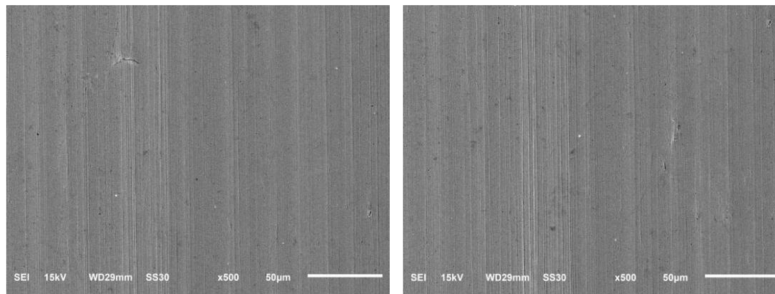
(f) 05#



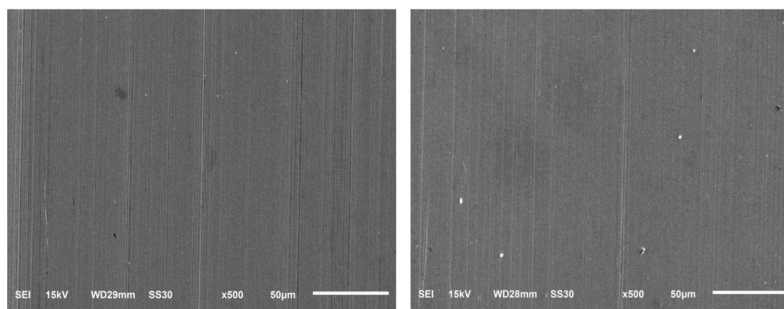
(g) 06#



(h) 07#



(i) 08#



(j) 09#

Fig. 13 continued.

**Acknowledgements** The authors would like to thank the National Natural Science Foundation of China No. NSFC 51206011 and U1937201, Jilin Province Science and Technology Development Program of Jilin Province No. 20200301040RQ, Project of Education Department of Jilin Province No. JJKH20190541KJ, and Changchun Science and Technology Program of Changchun City No. 18DY017.

**Author contribution** Weihong Zhao designed and performed the manuscript, analyzed the data, and drafted the manuscript. Jiyong Qu and Junye Li analyzed the data and supervised this study. Ningning Su and Guangfeng Shi conceived the project, and Jianhe Liu organized the paper and edited the manuscript. All authors read and approved the manuscript.

## Declarations

**Ethics approval** Not applicable.

**Consent to participate** Not applicable.

**Consent for publication** All presentations of case reports have consent for publication.

**Conflict of interest** The authors declare no competing interests.

## References

- Petare AC, Jain NK (2018) A critical review of past research and advances in abrasive flow finishing process. *Int J Adv Manuf Technol* 97(1-4):741–782. <https://doi.org/10.1007/s00170-018-1928-7>
- Sato T, Soh E, Nakayama Y, Shinagawa M, Fukuchi Y (2016) Effect of media degradation on finishing characteristics in abrasive flow machining. *Mater Sci Forum* 4389:127–132. <https://doi.org/10.4028/www.scientific.net/MSF.874.127>
- Sankar MR, Jain VK, Ramkumar J (2016) Nano-finishing of cylindrical hard steel tubes using rotational abrasive flow finishing (R-AFF) process. *Int J Adv Manuf Technol* 85(9-12):2179–2187. <https://doi.org/10.1007/s00170-015-8189-5>
- Fu YZ, Wang XP, Gao H, Gao H, Wei HB, Li SC (2016) Blade surface uniformity of blisk finished by abrasive flow machining. *Int J Adv Manuf Technol* 84(5-8):1725–1735. <https://doi.org/10.1007/s00170-015-8270-0>
- Duval-Chaneac MS, Han S, Claudin C, Salvatore F, Bajolet J, Rech J (2018) Experimental study on finishing of internal laser melting (SLM) surface with abrasive flow machining (AFM). *Precis Eng* 54:1–6. <https://doi.org/10.1016/j.precisioneng.2018.03.006>
- Singh S, Kumar D, Ravi Sankar MR, Jain VK (2019) Viscoelastic medium modeling and surface roughness simulation of microholes finished by abrasive flow finishing process. *Int J Adv Manuf Technol* 100(5-8):1165–1182. <https://doi.org/10.1007/s00170-018-1912-2>
- Li JY, Su NN, Wei LL, Zhang XM, Yin YL, Zhao WH (2019) Study on the surface forming mechanism of the solid–liquid two-phase grinding fluid polishing pipe based on large eddy simulation. *P I Mech Eng B-J Eng* 14:2505–2514. <https://doi.org/10.1177/0954405419841814>
- Silvis MH, Remmerswaal RA, Verstappen R (2017) Physical consistency of subgrid-scale models for large-eddy simulation of incompressible turbulent flows. *Phys Fluids* 29(1):015105. <https://doi.org/10.1063/1.4974093>
- Zhang Y, Kihara H, Abe KI (2017) On the effect of an anisotropy-resolving subgrid-scale model on large eddy simulation predictions of turbulent open channel flow with wall roughness. *J Turbul* 18(9):809–824. <https://doi.org/10.1080/14685248.2017.1333617>
- Linkmann M, Buzzicotti M, Biferale L (2018) Multi-scale properties of large eddy simulations: correlations between resolved-scale velocity-field increments and subgrid-scale quantities. *J Turbul* 19(6):493–527. <https://doi.org/10.1080/14685248.2018.1462497>
- Mao J, Zhang K, Liu K (2017) Comparative study of different subgrid-scale models for large eddy simulations of magnetohydrodynamic turbulent duct flow in OpenFOAM. *Comput Fluids* 152:195–203. <https://doi.org/10.1016/j.compfluid.2017.04.024>
- Wang AC, Cheng KC, Chen KY, Chen KY, Lin YC (2018) A study on the abrasive gels and the application of abrasive flow machining in complex-hole polishing. *Procedia Cirp* 68:523–528. <https://doi.org/10.1016/j.procir.2017.12.107>
- Li J, Ji SM, Tan DP (2017) Improved soft abrasive flow finishing method based on turbulent kinetic energy enhancing. *Chinese J Mech Eng* 30(2):301–309. <https://doi.org/10.1007/s10033-017-0071-y>
- Qi H, Wen DH, Yuan QL, Zhang L, Chen ZZ (2016) Numerical investigation on particle impact erosion in ultrasonic-assisted abrasive slurry jet micro-machining of glasses. *Powder Technol* 314:627–634. <https://doi.org/10.1016/j.powtec.2016.08.057>
- Awad E, Toorman E, Lacor C (2009) Large eddy simulations for quasi-2D turbulence in shallow flows: a comparison between different subgrid scale models. *J Mar Syst* 77(4):511–528. <https://doi.org/10.1016/j.jmarsys.2008.11.011>
- Ge JQ, Ji SM, Tan DP (2018) A gas-liquid-solid three-phase abrasive flow processing method based on bubble collapsing. *Int J Adv Manuf Technol* 95(1):1069–1085. <https://doi.org/10.1007/s00170-017-1250-9>
- Smagorinsky J (1963) General circulation experiments with the primitive equations. *Mon Weather Rev* 91(3):99–164. [https://doi.org/10.1175/1520-0493\(1963\)091<0099:GCEWTP>2.3.CO;2](https://doi.org/10.1175/1520-0493(1963)091<0099:GCEWTP>2.3.CO;2)
- Nicoud F, Ducros F (1999) Subgrid-scale stress modelling based on the square of the velocity gradient tensor. *Flow Turbul Combust* 62(3):183–200. <https://doi.org/10.1023/A:1009995426001>
- Shur ML, Spalart PR, Strelets MK, Travin AK (2008) A hybrid RANS-LES approach with delayed-DES and wall-modelled LES capabilities. *Int J Heat Fluid Fl* 29(6):1638–1649. <https://doi.org/10.1016/j.ijheatfluidflow.2008.07.001>
- Kim WW, Menon S (2013) Application of the localized dynamic subgrid-scale model to turbulent wall-bounded flows. 35th Aerospace Sciences Meeting and Exhibit. <https://doi.org/10.2514/6.1997-210>
- Miao C, Shafir SN, Lambropoulos JC, Mich J, Jacobs SD (2009) Shear stress in magnetorheological finishing for glasses. *Appl Opt* 48:2585–2594. <https://doi.org/10.1364/AO.48.002585>
- Jain RK, Jain VK, Dixit PM (1999) Modeling of material removal and surface roughness in abrasive flow machining process. *Int J Mach Tools Manuf* 39:1903–1923. [https://doi.org/10.1016/S0890-6955\(99\)00038-3](https://doi.org/10.1016/S0890-6955(99)00038-3)
- Li WH, Li XH, Yang SQ, Li WD (2018) A newly developed media for magnetic abrasive finishing process: material removal behavior and finishing performance. *J Mater Process Technol* 260:20–29. <https://doi.org/10.1016/j.jmatprotec.2018.05.007>
- Kathiresan S, Mohan B (2020) Multi-objective optimization of magneto rheological abrasive flow nano finishing process on AISI stainless steel 316L. *J Nano R* 63:98–111. <https://doi.org/10.4028/www.scientific.net/JNanoR.63.98>

**Publisher's note** Springer Nature remains neutral with regard to jurisdictional claims in published maps and institutional affiliations.